

A computational tool to improve flapping efficiency of robotic insects

Yufeng Chen, Alexis Lussier Desbiens, and Robert J Wood

Abstract— We implement a 2D computational model to investigate the unsteady aerodynamic effects not captured by classical quasi-steady models. We compare numerical simulation results, experimental measurements and quasi-steady predictions to demonstrate the strength of the numerical tool in identifying unsteady fluid mechanisms and improving propulsive efficiency of flapping wing robots. In particular, this study quantifies the effect of the relative phase between wing degrees of freedom δ on lift and drag production. The computational model also identifies unsteady effects such as wake capture and downwash that are not accounted for in classical quasi-steady models. To examine the accuracy of our computational model, we fabricate millimeter-scale wings through the SCM fabrication processes and measure flapping kinematics and dynamics. The experiments show 2D computational model is 44% more accurate than the quasi-steady model and can be further used to improve wing morphology for better aerodynamic performance.

I. INTRODUCTION

In recent years a number of flapping-wing micro-air-vehicles have achieved stable hovering flight [1], [2], [3]. Compared to traditional fixed wing or helicopter flight, flapping wing flight observed in nature relies on unsteady fluid dynamics principles to achieve better maneuverability and smaller vehicle size [4]. Such advantages make flapping wing air vehicles excellent candidates for surveillance and remote sensing in hazardous locations. Meanwhile, the unsteady nature of flapping flight poses modeling and control challenges to improve stability, maneuverability, and propulsive efficiency.

The current Harvard RoboBee design, shown in Figure 1, uses two bimorph piezoelectric actuators to independently control wing stroke motion, and the hinge motion is mediated by passively rotating Kapton hinges. While this design reduces system complexity, power consumption and vehicle mass, it poses challenges to developing a dynamical model that predicts both wing hinge kinematics and thrust generation.

A number of quasi-steady models have been developed from steady state classical aerodynamics [5] to describe flapping flight. In 1963, Von Karman et al. first proposed a formula for lift and drag coefficients based on complete separated flow computation. In 2002, Dickinson et al. [6] observed unsteady phenomena such as rotational circulation

These authors are with the School of Engineering and Applied Sciences, Harvard University, Cambridge, MA 02138, USA, and the Wyss Institute for Biologically Inspired Engineering, Harvard University, Boston, MA, 02115, USA (email: yufengchen,desbiens,rjwood@seas.harvard.edu)

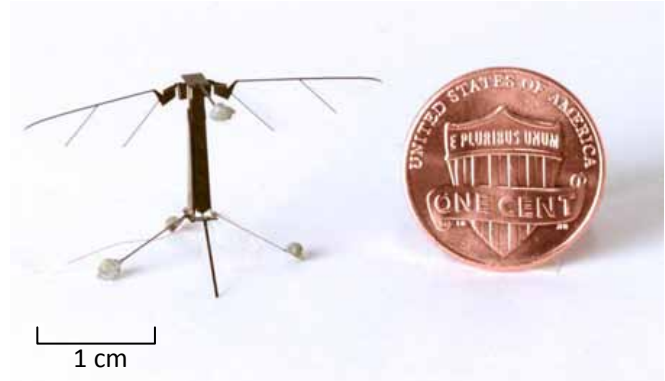


Fig. 1. The current Harvard RoboBee is an 80mg flapping wing microrobot that can lift an extra 50mg payload. The wing design and control algorithm are based on quasi-steady models that predict time averaged forces and torques.

and delayed stall using a robotic wing. He proposed a quasi-steady model based on his experimental results and introduced additional modeling terms that account for added mass and rotational damping effects. Lussier Desbiens et al. [7] adopted the quasi-steady model for a passive flapping system and demonstrated that the quasi-steady model yields accurate kinematic and thrust predictions in the time averaged sense. However, quasi-steady models cannot yield accurate predictions of time varying lift and drag, and this error in turn affects prediction of aerodynamic torques that govern hinge kinematics. This modeling insufficiency restricts all control algorithms to rely on time-averaged predictions, which adversely affects maneuverability and flapping efficiency.

A number of 2D [8] or 3D [9] numerical models have been developed to bridge the discrepancy between experiments and quasi-steady models. Lentink et al. [10] show that 3D mechanisms such as spanwise flow stabilize the leading edge vortex and delay detachment. In hovering flight, vortex shedding only happens at stroke reversal and as a result 2D and 3D computational models yield very similar predictions. In this paper, we implement a numerical two dimensional Navier Stokes equation solver to study effects of parameters that are not treated by quasi-steady models. In particular, we investigate the effect of relative phase between stroke and hinge rotation angles δ (Figure 2) on lift and drag production. As shown in Dickinson's robotic wing experiments [6], moderate differences in δ accounts for more than 30% difference in measured lift. Current wing and hinge designs rely on quasi-steady models to optimize kinematic parameters such as stroke and hinge amplitude, but ignore the influence of

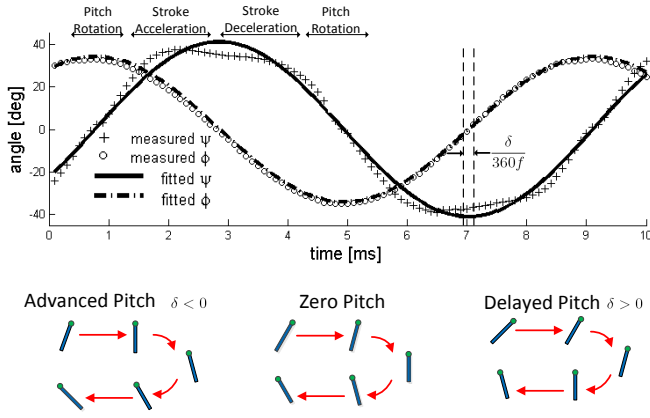


Fig. 2. The top graph shows measured stroke and hinge angles and the least squares fit to a pure sinusoid. The recorded motion is nearly purely sinusoidal, and δ indicates the relative phase between stroke and hinge motion. If $\delta = 0^\circ$, then the hinge angle is 0° at maximum stroke, as shown in the bottom middle figure. $\delta < 0^\circ$ means wing rotation leads stroke motion and $\delta > 0^\circ$ means wing rotation lags behind stroke motion. Intervals of large stroke angle (ϕ) represent pitch rotation, and intervals of slowly changing hinge angle (ψ) represents wing translation. The wing translational phase is further divided into stroke acceleration and stroke deceleration phase based on the curvature of the stroke function. The motion tracking method is described in Section IIIB.

δ . We study this parameter's influence on lift and drag production by running simulations and experiments, thereby extracting useful physical principles that will improve future wing and hinge designs. The simulated results using our CFD solver are compared with experimental results to validate our findings. This computational model is shown to be 44% more accurate than traditional quasi-steady models.

In addition, our simulation shows several interesting unsteady phenomena such as vortex shedding, downwash and wake capture. These physical phenomena affect lift and drag production but are not accounted for in quasi-steady models. By choosing appropriate morphological parameters, we can increase lift production by making effective use of the wake capture process. Hence, unlike quasi-steady models that only yield force predictions, our numerical model allows us to improve wing morphology and motion by making effective use of unsteady phenomena. Owing to this increased accuracy, this numerical tool is more powerful for improving flapping efficiency than its quasi-steady counterparts. In the rest of this paper we explain the implementation of the numerical model, describe the experiment procedure, and compare simulation with experimental results.

II. COMPUTATIONAL METHOD

A. Flapping Kinematics

As shown in Figure 3, the kinematics of a flapping wing has 2 degrees of freedom—stroke and hinge rotations. The experimental set up allows us to control the frequency and amplitude of stroke motion, while the hinge rotation is passively controlled by aerodynamic and inertial torques and hinge compliance. As shown in Figure 2, experimental measurement shows the hinge motion is very close to be a

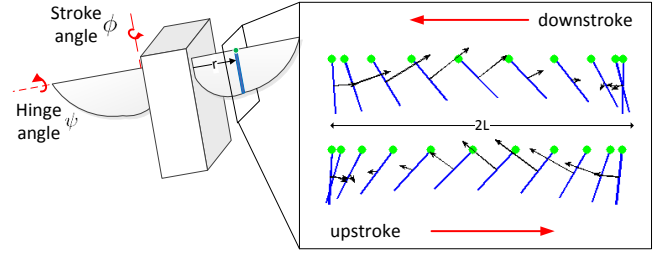


Fig. 3. The RoboBee wing has 2 degrees of freedom. The rotation (ϕ) around the vertical body axis is actively controlled by piezoelectric actuators, and the rotation (ψ) around wing hinge line is passive. In blade element method, the motion of a thin rectangular segment along the wing chord (shown in blue) is projected onto a 2D plane. The leading edge of the wing segment is marked green. The angular stroke motion is transformed into planar oscillatory motion, in which the amplitude L is given by $L = \phi_{max}r$, and r is half the wing radius. The black arrows indicate the instantaneous direction and relative amplitude of aerodynamic forces.

pure sinusoid. Mathematically, the stroke and hinge motion are given by

$$\begin{aligned}\phi &= \phi_{max} \sin(\omega t) \\ \psi &= \psi_{max} \cos(\omega t + \delta),\end{aligned}\quad (1)$$

where ϕ_{max} is the stroke amplitude, ψ_{max} is the hinge amplitude and δ is the relative phase. In quasi-steady blade element models and 2D computational fluid dynamics models, the angular stroke motion is approximated by the translational motion of a thin blade element located a distance r from the wing root. As shown in Figure 3, the amplitude of the wing chord translational motion is given by $L = r\phi_{max}$, where r is chosen to be the wing midspan.

Previous experiments have shown that mean lift increases when $\delta < 0^\circ$ and decreases when $\delta > 0^\circ$ [6], [7]. As shown in Figure 2, $\delta < 0^\circ$ corresponds to advanced passive rotation and $\delta > 0^\circ$ corresponds to delayed passive rotation. Current quasi-steady models cannot accurately predict the effect of varying the kinematic parameter δ , hence we aim to investigate the influence of this parameter using computational tools.

B. Numerical solver implementation

Our computational model assumes a 2D thin flat plate of dimension $20\mu m \times 3mm$ flapping in air with kinematics described in the previous section. The two dimensional incompressible Navier Stokes equation and the corresponding boundary conditions that govern the flapping motion are :

$$\begin{aligned}\rho \frac{\partial \bar{u}}{\partial t} + \rho(\bar{u} \cdot \bar{\nabla})\bar{u} &= -\bar{\nabla}p + \mu \nabla^2 \bar{u} \\ \bar{\nabla} \cdot \bar{u} &= 0 \\ \bar{u}|_{wing} &= (u, v)|_{wing} \\ p|_{\infty} &= 0,\end{aligned}$$

where $\bar{u} = (u, v)$ is the fluid velocity field and p is the pressure field that enforces the incompressibility condition. The fluid speed along the wing surface is equal to the wing velocity, and the pressure at far field is set to be 0. In our

computations, the range of Reynolds number is between 300 to 600.

We implement a numerical solver using the nodal discontinuous Galerkin finite element method, which allows more geometric flexibility than the finite difference method and requires coarser mesh resolution than the continuous Galerkin method. The solver is implemented on a moving Cartesian coordinate system, and the computational Delaunay triangulation mesh is generated by the open source package distmesh [13]. The circular mesh used for simulation contains 2242 elements, and its radius is chosen to be six times the wing chord length to avoid unintended boundary effects. The solution inside each mesh element is interpolated using 5th order Lagrange polynomials.

The structure of this solver is based on the method developed in [11]. The temporal scheme is solved using the second order backward Adams Bashforth method, and the spatial scheme is separated into three steps that individually treat nonlinear advection, pressure field contribution, and viscous correction. In addition, the flapping motion requires the computational mesh to move with respect to the inertial reference frame, hence a change of coordinate system is needed. This method is not identical to solving the Navier Stokes equation in a non-inertial reference frame by adding fictitious forces; it is more general because it also allows geometric deformation of the mesh. The transformation between physical coordinates that are fixed in space and computational coordinates that move with the wing is defined as:

$$\begin{aligned} u(x, y, t) &= \tilde{u}(\zeta, \eta, \tau) \\ v(x, y, t) &= \tilde{v}(\zeta, \eta, \tau) \\ p(x, y, t) &= \tilde{p}(\zeta, \eta, \tau) \end{aligned} \quad (2)$$

We denote the physical coordinates by x and y and the computational coordinates by ζ and η . The temporal variables t and τ are identical, however we use different symbols to avoid confusion between $\frac{\partial}{\partial t}$ and $\frac{\partial}{\partial \tau}$. The operators in the inertial reference frame are replaced by operators in the moving frame:

$$\begin{aligned} \frac{\partial}{\partial t} &= \frac{\partial \zeta}{\partial t} \frac{\partial}{\partial \zeta} + \frac{\partial \eta}{\partial t} \frac{\partial}{\partial \eta} + \frac{\partial}{\partial \tau} \\ \frac{\partial}{\partial x} &= \frac{\partial \zeta}{\partial x} \frac{\partial}{\partial \zeta} + \frac{\partial \eta}{\partial x} \frac{\partial}{\partial \eta} \\ \frac{\partial}{\partial y} &= \frac{\partial \zeta}{\partial y} \frac{\partial}{\partial \zeta} + \frac{\partial \eta}{\partial y} \frac{\partial}{\partial \eta} \end{aligned} \quad (3)$$

In component form, the Navier Stokes equation is trans-

formed to :

$$\begin{aligned} \frac{\partial u}{\partial \tau} &= -\frac{\partial u}{\partial \zeta} \zeta_t - \frac{\partial u}{\partial \eta} \eta_t - u \left(\zeta_x \frac{\partial u}{\partial \zeta} + \eta_x \frac{\partial u}{\partial \eta} \right) \\ &\quad - v \left(\zeta_y \frac{\partial u}{\partial \zeta} + \eta_y \frac{\partial u}{\partial \eta} \right) - \frac{1}{\rho} \left(\zeta_x \frac{\partial p}{\partial \zeta} + \eta_x \frac{\partial p}{\partial \eta} \right) \\ &\quad + \nu \left(\zeta_x^2 \frac{\partial^2}{\partial \zeta^2} + \eta_x^2 \frac{\partial^2}{\partial \eta^2} + \zeta_y^2 \frac{\partial^2}{\partial \zeta^2} + \eta_y^2 \frac{\partial^2}{\partial \eta^2} \right) u \\ &\quad + 2\nu(\eta_x \zeta_x + \eta_y \zeta_y) \frac{\partial}{\partial \zeta} \frac{\partial}{\partial \eta} u \\ \frac{\partial v}{\partial \tau} &= -\frac{\partial v}{\partial \zeta} \zeta_t - \frac{\partial v}{\partial \eta} \eta_t - u \left(\zeta_x \frac{\partial v}{\partial \zeta} + \eta_x \frac{\partial v}{\partial \eta} \right) \\ &\quad - v \left(\zeta_y \frac{\partial v}{\partial \zeta} + \eta_y \frac{\partial v}{\partial \eta} \right) - \frac{1}{\rho} \left(\zeta_y \frac{\partial p}{\partial \zeta} + \eta_y \frac{\partial p}{\partial \eta} \right) \\ &\quad + \nu \left(\zeta_x^2 \frac{\partial^2}{\partial \zeta^2} + \eta_x^2 \frac{\partial^2}{\partial \eta^2} + \zeta_y^2 \frac{\partial^2}{\partial \zeta^2} + \eta_y^2 \frac{\partial^2}{\partial \eta^2} \right) v \\ &\quad + 2\nu(\eta_x \zeta_x + \eta_y \zeta_y) \frac{\partial}{\partial \zeta} \frac{\partial}{\partial \eta} v \\ 0 &= \zeta_x \frac{\partial u}{\partial \zeta} + \eta_x \frac{\partial u}{\partial \eta} + \zeta_y \frac{\partial v}{\partial \zeta} + \eta_y \frac{\partial v}{\partial \eta} \end{aligned} \quad (4)$$

where ζ_t , η_t are the speed of the computational coordinates with respect to inertial reference coordinates x and y , and ζ_x , η_x , ζ_y and η_y are components of the transformation Jacobian between physical and computational coordinates. The parameters ρ and ν represent fluid density and kinematic viscosity. The boundary conditions of u , v and p remain unchanged. Given the fluid velocity field and pressure field we can compute the force per unit length and torque per unit length on the wing segment by integrating the stress tensor along the wing surface as: $\vec{F} = \int_{wing} \hat{n} \cdot \vec{\sigma} dl$, and $\vec{T} = \int_{wing} \vec{r} \times \hat{n} \cdot \vec{\sigma} dl$, where \hat{n} is the local surface normal. We can expand the stress tensor and arrive at equations for lift and drag forces as follows:

$$\begin{aligned} F_D &= - \int_{wing} \left(-pn_x + 2\nu\rho \frac{\partial u}{\partial x} n_x + \nu\rho \frac{\partial v}{\partial x} n_y + \nu\rho \frac{\partial u}{\partial y} n_y \right) dl \\ F_L &= - \int_{wing} \left(-pn_y + \nu\rho \frac{\partial u}{\partial y} n_x + \nu\rho \frac{\partial v}{\partial x} n_y + 2\nu\rho \frac{\partial v}{\partial y} n_y \right) dl. \end{aligned} \quad (5)$$

Finally, we can relate the computational model to the quasi-steady model by computing lift and drag coefficients:

$$\begin{aligned} C_L &= \frac{F_L}{\frac{1}{2}\rho u_{rms}^2 c} \\ C_D &= \frac{F_D}{\frac{1}{2}\rho u_{rms}^2 c}, \end{aligned} \quad (6)$$

where u_{rms} is the root mean square of wing velocity and c is the wing chord length.

III. EXPERIMENT SETUP

To compare the numerical model with the actual forces generated by the RoboBee, we utilize an existing set up to measure the kinematics and dynamics of a flapping wing [7]. As shown in Figure 4, the wing is attached to a custom made carbon fiber wing driver that is mounted on a dual axis force sensor. The wing stroke motion is controlled by a bimorph piezoelectric actuator, and the hinge motion is passively mediated by a Kapton hinge. The optical sensor records the motion of the piezoelectric actuator, and the camera records the top view of the flapping motion. The following sections describe the details of force measurement, motion measurement, and wing fabrication processes.

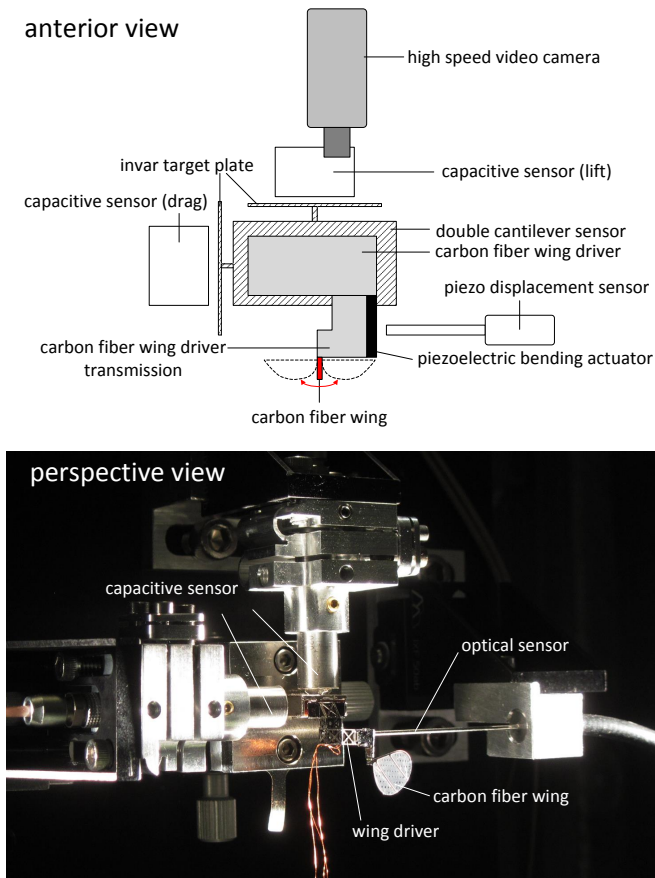


Fig. 4. This illustration shows the experimental setup. The carbon fiber wing driver consists of a piezoelectric actuator (black), transmission and structural support. An external electric signal controls the actuator to drive the stroke motion of the millimeter-scale wing (red). The aerodynamic and inertial forces generated by a flapping wing are transformed into displacements of the Invar sensor. Two capacitive sensors measure the displacement and the data is post-processed to obtain lift and drag. A high speed camera records the stroke motion.

A. Force measurement

The custom sensor consists of four parallel dual cantilever modules arranged in a series-parallel configuration. The structure converts a load into displacements in the vertical and horizontal directions, and the displacements in both directions are measured by two PISeCa D-510.021 capacitive sensors. We calibrate the sensors by hanging weights, and the sensitivity was found to be -84.6 and 85.5 V/mN for the lift and drag axes respectively. In our experiment, the driving frequency is chosen to be 120Hz so that lift force has a fundamental frequency of 240Hz and drag force has a fundamental frequency of 120Hz . Since the sensors measure aerodynamic and the inertial forces from the wing and wing driver, we only report time averaged drag measurements. On the other hand, we can accurately measure lift by filtering out 10Hz to 200Hz and $> 500\text{Hz}$ harmonics to eliminate actuator inertial contributions and system resonance. This band pass filter may eliminate higher order harmonics of the actual lift signal, hence for comparison purposes we also apply the same filter to the numerically computed lift.

The wing used in our experiment weigh 0.52mg , and the magnitude of wing inertial contribution often accounts for $15\% - 20\%$ of the aerodynamic contribution. Using measured flapping kinematics and the estimated mass properties from SolidWorks, we can subtract out the effect of wing inertial contribution. In the lift axis, the formula is given by

$$F_{aero} = ma_z - mg - F_{sensor}, \quad (7)$$

where a_z is the z -component of wing inertial acceleration. We can compute a_z as

$$a_z = r_{com,z}(\cos(\psi)\ddot{\psi}^2 + \sin(\psi)\ddot{\psi}), \quad (8)$$

where $r_{com,z}$ is the wing center of mass position in the z -direction. In our mass model we neglect the center of mass offset due to wing thickness.

B. Wing kinematics measurement

The wing stroke and hinge motion are recorded at 10kHz using a Phantom V7.3 high speed video camera with an AF MICRO Nikon 200mm $f/4$ lens. In this experiment, we treat the wing as a flat plate and use the top view to extract hinge and stroke motions. The details of the extraction algorithm are described in [7].

C. Wing and wing hinge design

The wing used in the experiment is made from a carbon fiber frame and polyester membrane with 3mm mean chord and 54mm^2 total area. The wing hinge is made of a compliant $1.25\text{mm} \times 140\mu\text{m} \times 7\mu\text{m}$ kapton layer sandwiched between two carbon fiber layers. Details of the design and manufacturing methodology used for the wing, transmission, and actuators are described in [14].

IV. DISCUSSION

To examine the validity of our numerical model, we compare simulation results with the measurements. A wing is flapped with specified driving voltage and frequency pairs and we measure the corresponding kinematics and forces. The measured wing kinematics are used as the inputs to the numerical simulation, and lift and drag coefficients are computed to compare with experimental results. The numerical simulator is also used to explore parameter spaces that are not covered by passive rotation experiments to further study the influence of relative phase parameter δ and identify phenomena not accounted for in quasi-steady models.

A. Comparison between experiment and computation

We run the flapping experiment with a 120Hz driving frequency and sweep through different voltage amplitudes to find a case for which the relative phase δ between stroke and hinge angle is 0° . The kinematics and forces are measured using the method described in the previous section. At 190V , δ is measured to be -0.19° and the flapping stroke and

hinge amplitudes are measured to be 34° and 43° degrees respectively. The corresponding Reynolds number is

$$Re = \frac{u_{max}\bar{c}}{\nu} = 570 \quad (9)$$

We then use $\Phi_{max} = 34^\circ$, $\Psi_{max} = 43^\circ$, and $\delta = 0^\circ$ as the input parameters and solve the 2D flow problem for the chord segment at midspan of the wing. Finally, we compute the instantaneous lift and drag coefficients and compare that with classical quasi-steady model and experimental measurements.

As shown in the top graph of Figure 5, the numerical solution (blue) shows lift peaks in the stroke deceleration phase and this agrees well with the measurement (red). On the other hand, the green curve (quasi-steady model) is symmetric with respect to its local maxima so the quasi-steady model does not distinguish between the stroke acceleration phase and the stroke deceleration phase. While there are quasi-steady models based on 2D inviscid flow that address added mass and rotational circulation effects, they usually involve extra fitting parameters and are not robust for large operating range. Hence, the quasi-steady model we compare with only contains the translational term. This asymmetry can be understood by studying the flow structures around the wing and can be utilized to enhance lift production. Figure 6 shows the vorticity field around a flapping wing segment in the fourth flapping period. Large vorticity on the wing leading edge corresponds to high lift. In the stroke acceleration phase ($T=3.08$ to $T=3.25$ and $T=3.58$ to $T=3.75$), vorticity on the upper wing surface is small. In the stroke deceleration phase ($T=3.25$ to $T=3.42$ and $T=3.75$ to $T=3.91$) we observe a large vortex on the upper wing surface that leads to large lift force. We also observe that the leading edge vortex grows only when the angle of attack is positive. On the other hand, the vortex shedding process is not sensitive to angle of attack.

This observation suggests that by varying the relative phase δ between stroke and hinge angles we can increase or reduce lift. $\delta < 0^\circ$ corresponds to advanced wing pitch so that the leading edge vortex starts to grow immediately after stroke reversal at a positive angle of attack. These kinematics favor vortex development and augment lift production. In contrast, $\delta > 0^\circ$ corresponds to delayed wing pitch and inhibits vortex generation. Figure 7 shows the negative correlation between time averaged lift coefficient \bar{C}_L and time averaged drag coefficient \bar{C}_D as functions of δ . In the classical quasi-steady model, C_L and C_D only depend on angle of attack α . However, using the numerical solver we have shown that lift and drag coefficients are also strong functions of δ . Compared to $\delta = 0^\circ$, the simulation of $\delta = -30^\circ$ shows 30% increase of \bar{C}_L and 44% increase of \bar{C}_D (Figure 7B). On the other hand, at $\delta = 30^\circ$ we observe 47% decrease of \bar{C}_L and 9.7% decrease of \bar{C}_D (Figure 7B). This computational result agrees with the qualitative experiment result presented in [12]. Not only does the numerical model describe the influence of the kinematic parameter δ , it also shows other unsteady effects that can be utilized to improve

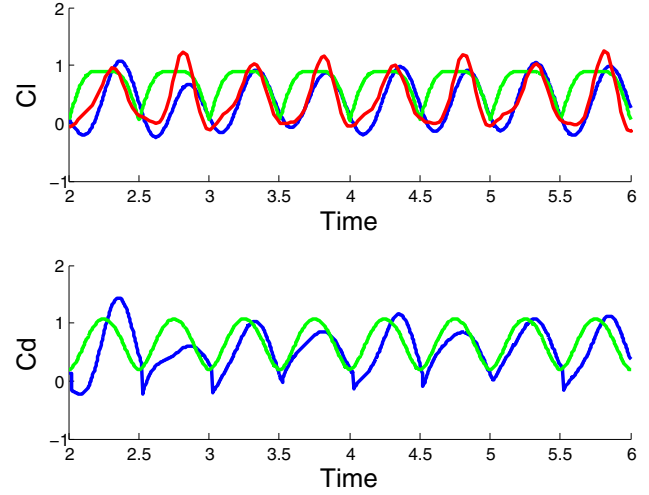


Fig. 5. Lift and drag coefficients for 120Hz with $\delta = 0^\circ$, $\phi_{max} = 35^\circ$, and $\psi_{max} = 43^\circ$. The x-axis is the number of flapping periods. To avoid transient effects, this graph shows the lift and drag coefficient from the 3rd to the 6th flapping periods. The blue curves represent the numerical solution by solving the 2D Navier Stokes equation. The green curve shows quasi-steady estimates (based on Dickinson's formula [6]) and the red curve shows sensor measurements. To eliminate wing driver inertial contributions and sensor resonance, the 10 to 200Hz and $> 500\text{Hz}$ harmonics are filtered out. The same filter is applied to the numerically computed forces. The wing inertial contribution is also subtracted out from the sensor measurement. We do not show the time varying drag measurement because the motion of piezo-actuator is in the direction of the drag axis.

flapping kinematics and wing morphology.

B. Identification of unsteady effects

Downwash effect: Our simulation shows that an impulsively started wing generates more lift than that of a wing already flapped for several periods. Since the kinematics in both cases are identical, the quasi-steady model predicts identical lift and drag. However, as shown in Figure 8, the pressure on the wing leading edge at $T = 0.25$ is more negative than it is at $T = 2.25$, meaning that the instantaneous lift generated is larger at $T = 0.25$. This phenomenon can be understood by comparing the y-component of the velocity field. A flapping wing continuously generates lift and transfers downward momentum to surrounding fluid. This downwash tends to reduce the translational lift generated by the wing. In our simulation, the lift of the first period is 17% higher than the time-averaged lift.

Generation and shedding of vortices: A leading edge vortex develops in the stroke acceleration phase and sheds at the end of stroke deceleration phase. As discussed in the previous section, this physical mechanism depends on flow field history and cannot be modeled by classical quasi-steady models. Figure 9 shows the vorticity field and the corresponding pressure field to illustrate vortex generation and vortex shedding processes. We can increase or reduce mean lift by varying the phase lag δ between stroke translation and pitch rotation.

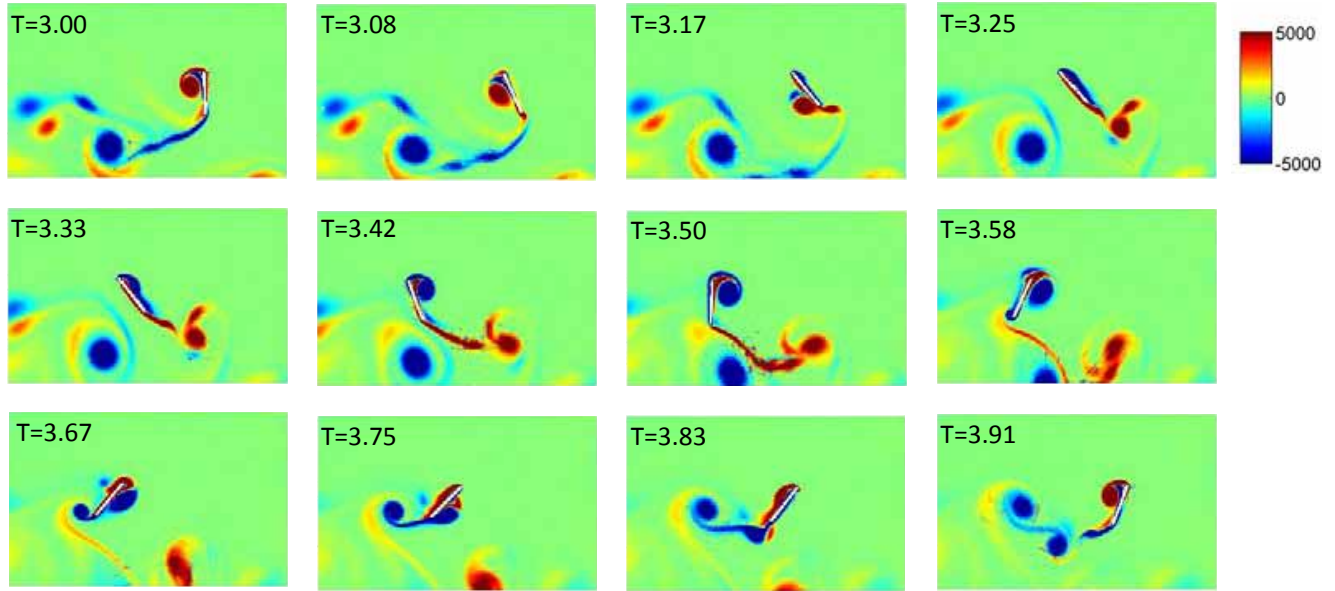


Fig. 6. Vorticity plot around a flapping wing in the fourth period. Red color represents positive vorticity (points out of the page) and blue color represents negative vorticity (points into the page). The vorticity color bar has units of $1/s$. Since the flow is incompressible, the information shown by the vorticity field is equivalent to that of the complete velocity field. Regions of high vorticity (absolute value) correspond to regions of low pressure. A large vortex grows on the leading edge of a translating wing and is shed during stroke reversal. A lift peak occurs near $T=3.42$ and $T=3.91$ during the stroke deceleration phase.

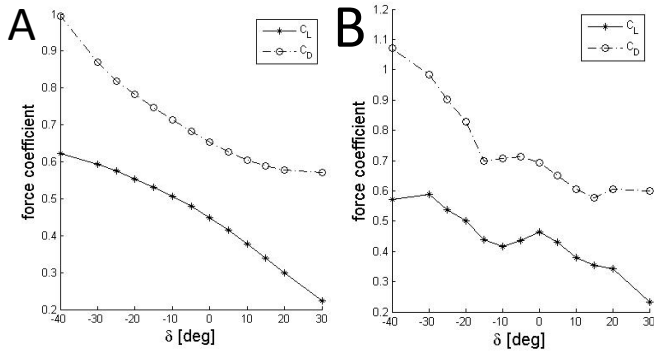


Fig. 7. \bar{C}_L and \bar{C}_D as functions of δ . All simulations are ran with identical mesh, stroke and hinge amplitude, while the phase parameter δ is varied from -40° to 30° . The graph on the left (A) shows time averaged lift and drag coefficients for an impulsively started wing for a half flapping period. The graph on the right (B) shows the same simulations for 4 flapping periods. In the first half stroke there is no wake capture and downwash effects so Figure 7A quantifies the effect of δ on translational lift and drag alone. After the first half flapping period we observe interaction between wing and shed vortices. Figure 7B shows variations of \bar{C}_L and \bar{C}_D due to δ 's effect on both translational and rotational motion.

Wake capture: Wake capture refers to the interaction between a wing and its previously shed vortex in the stroke acceleration phase. As described in [4], wake capture can often lead to a secondary lift peak. In our simulation, wake capture is beneficial to lift generation in the first period but becomes detrimental to lift generation for subsequent flapping periods. As shown in Figure 5, the computed lift coefficient is negative in the stroke acceleration phase. We

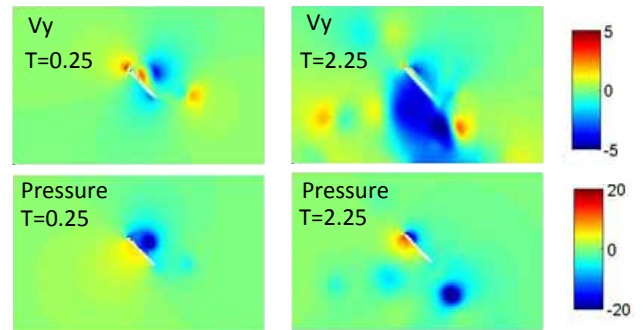


Fig. 8. Downwash and its adverse effect on lift production. The figures in the first row show the y -component of the velocity field. The velocity field color bar has units of m/s . More severe downward flow (blue) is observed at $T=2.25$ than at $T=0.25$. Figures in the second row show that the pressure field on the wing upper surface is smaller at $T=0.25$ than at $T=2.25$, which correspond to higher lift at $T=0.25$. The pressure field color bar has units of N/m^2 .

can understand this phenomenon by studying pressure and vorticity graphs shown in Figure 10. At $T = 0.5$ and $T = 1.5$ we observe similar shed vortices. In the first period, the shed vortex moves over the leading edge and convects to the opposite side of the wing at $T = 0.7$. The corresponding pressure graphs show that the region of low pressure convects to the wing upper surface, thus creating more lift. On the other hand, the vortex shed at $T = 1.5$ moves along the lower wing surface and convects toward the trailing edge. As a result, a low pressure region along lower surface corresponds to lower lift. This phenomenon can be

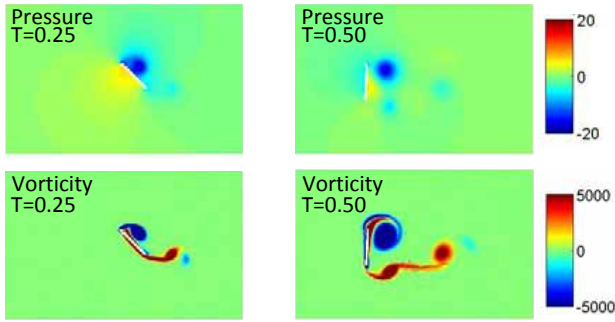


Fig. 9. Vortex generation and shedding. The figures in the first row show the pressure field around a translating ($T=0.25$) or rotating ($T=0.50$) wing. The figures in the second row show the corresponding vorticity field. During wing translation ($T=0.25$), a leading edge vortex grows and as a result a low pressure region on the wing upper surface leads to high lift. During wing rotation, the vortex detaches from the wing surface ($T=0.50$) and lift plummets. The pressure field has units of N/m^2 and the vorticity field has units of $1/s$.

explained by the downwash effect, in which the downward moving fluid affects the vortex convection direction.

Through simulations, we find that wake capture properties can be enhanced by increasing stroke amplitude or shrinking wing chord. Figure 11A compares vorticity plots of flapping motions with different stroke amplitudes. The shed vortex convects along lower wing surface for $L = 4mm$, and it convects to the upper wing surface for $L = 6mm$. The corresponding lift coefficients for a half flapping period ($T = 2$ to 2.5) is shown in Figure 11 B. While the primary lift peaks in both cases are similar, we observed different wake capture effects. During the stroke acceleration phase, the lift coefficient for $L = 4mm$ is negative while the lift coefficient for $L = 6mm$ is positive. As discussed in the previous section, this difference depends on whether the shed vortex convects along the lower wing surface or rolls over to the upper surface. We find that favorable wake capture leads to 32% increase of mean lift coefficient. This simulation result implies that future wing design must have appropriate stroke amplitude to chord length ratio to achieve favorable wake capture effects.

V. CONCLUSION AND FUTURE WORK

This paper presents a computational tool designed specifically to model the aerodynamic performance of RoboBee flapping flight. Unlike classical quasi-steady models that calculate aerodynamic forces based only on wing geometry and kinematics, this numerical model identifies unsteady fluid mechanisms that are important to improving propulsive efficiency. More specifically, we quantify the effect of the phase parameter δ on lift and drag production through simulations. While holding other kinematic parameters constant, the mean lift coefficient \bar{C}_L increases by 30% and mean drag coefficient increases by 44% if δ is reduced to $\delta = -30^\circ$. On the other hand, if δ is increased to $\delta = 30^\circ$ then we observe 47% decrease in mean lift coefficient and 9.7% decrease in

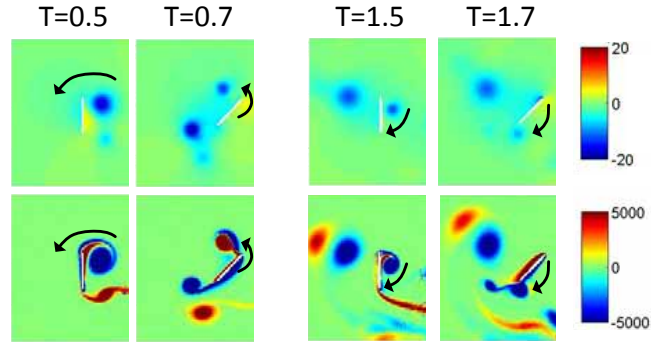


Fig. 10. Wake capture effect. Figures in the first row show vorticity plots with units of $1/s$ and figures in the second row show pressure field with units of N/m^2 . The figures on the left show a favorable wake capture effect in the first flapping period in which the vortex rolls over the leading edge and its corresponding low pressure acts to increase lift. The four figures on right show an adverse wake capture effect in the second period in which the vortex rolls along the lower wing surface and its corresponding low pressure region reduces lift.

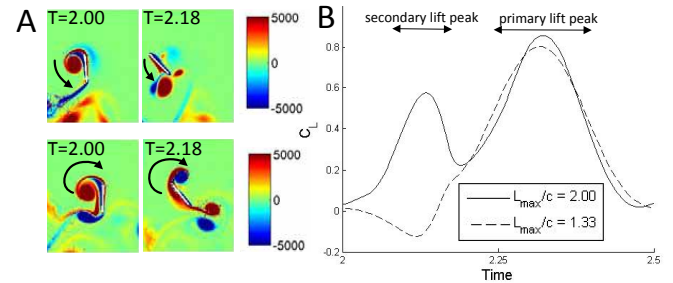


Fig. 11. Wake capture effects of different flapping amplitude to chord length ratio. The vorticity plots (A) illustrate different directions of vortex movement for $\frac{L}{c} = 1.33$ (top row) and $\frac{L}{c} = 2.00$ (bottom row). In the case of $\frac{L}{c} = 1.33$, the previously shed vortex convects along the lower wing surface. In the case of $\frac{L}{c} = 2.00$, the vortex rolls over to the upper wing surface. The lift coefficient graph (B) compares the time varying lift coefficients for a half flapping period. Whereas the primary translational lift peaks ($T=2.2$ to $T=2.5$) are similar, the secondary lift peaks ($T=2.0$ to $T=2.2$) are different due to differences in the wake capture process. The lift coefficient graph shows larger $\frac{L}{c}$ ratio corresponds to larger mean lift coefficient.

mean drag coefficient. This simulation result suggests that future RoboBee design should utilize a stiff hinge to advance passive wing pitch rotation. This computational result agrees well with previous experimental findings [7].

In addition, our simulations show that wake capture effects can be beneficial or detrimental to lift production depending on the movement of shed vortices. We can induce favorable wake capture effects by increasing the flapping amplitude to chord length ratio $\frac{L}{c}$. Furthermore, we have validated our numerical model by comparing simulation results to quasi-steady predictions and experimental measurement. It is shown that our numerical model gives a 44% percent better approximation to 3D experiments than the quasi-steady model in the least squares sense.

Whereas the quasi-steady model requires fitting coefficients, this numerical model is rigorously derived from Navier Stokes equations and does not require fitting pa-

rameters. This property makes the numerical model more reliable for future wing kinematics optimization studies. Ensuing studies should further develop this computational tool to optimize passive rotation kinematics. Whereas the current model requires completely prescribing stroke and hinge motion, the immersed boundary method can be implemented to allow wing-fluid interaction [15]. By defining wing stroke kinematics alone, future computational model should return hinge kinematics along with force estimates. In addition, particle image velocimetry techniques can be used to compare experiment measurement with the computed flow field.

VI. ACKNOWLEDGMENT

This work was partially supported by the National Science Foundation (award number CCF-0926148), and the Wyss Institute for Biologically Inspired Engineering. Any opinions, findings, and conclusions or recommendations expressed in this material are those of the authors and do not necessarily reflect the views of the National Science Foundation.

REFERENCES

- [1] K. Ma, P. Chirarattanon, S. Fuller, and R.J. Wood, "Controlled Flight of a Biologically Inspired, Insect-Scale Robot", *Science*, vol. 340, pp. 603-607, 2013.
- [2] Lentink, David, Stefan R. Jongerius, and Nancy L. Bradshaw. "The scalable design of flapping micro-air vehicles inspired by insect flight." In *Flying Insects and Robots*, pp. 185-205. Springer Berlin Heidelberg, 2010.
- [3] Keennon, Matthew, Karl Klingebiel, Henry Won, and Alexander Andriukov. "Development of the Nano Hummingbird: A Tailless flapping wing micro air vehicle." In *50th AIAA Aerospace Sciences Meeting including the New Horizons Forum and Aerospace Exposition*, pp. 1-24. 2012.
- [4] Shyy, Wei. *Aerodynamics of low Reynolds number flyers*. Vol. 22. Cambridge University Press, 2008.
- [5] Anderson, John David. *Fundamentals of aerodynamics*. Vol. 2. New York: McGraw-Hill, 2001.
- [6] Dickinson, Michael H., Fritz-Olaf Lehmann, and Sanjay P. Sane. "Wing rotation and the aerodynamic basis of insect flight." *Science* 284, no. 5422 (1999): 1954-1960.
- [7] A.L. Desbiens, Y. Chen, and R.J. Wood, "Wing characterization method for flapping wing micro air vehicle", *IEEE/RSJ Int. Conf. on Intelligent Robots and Systems*, Tokyo, Japan, Nov., 2013.
- [8] Wang, Z. Jane, James M. Birch, and Michael H. Dickinson. "Unsteady forces and flows in low Reynolds number hovering flight: two-dimensional computations vs robotic wing experiments." *Journal of Experimental Biology* 207, no. 3 (2004): 449-460.
- [9] Zheng, Lingxiao, Tyson L. Hedrick, and Rajat Mittal. "A multi-fidelity modelling approach for evaluation and optimization of wing stroke aerodynamics in flapping flight." *Journal of Fluid Mechanics* 721 (2013): 118-154.
- [10] Lentink, David, and Michael H. Dickinson. "Rotational accelerations stabilize leading edge vortices on revolving fly wings." *Journal of Experimental Biology* 212, no. 16 (2009): 2705-2719.
- [11] Hesthaven, Jan S., and Tim Warburton. *Nodal discontinuous Galerkin methods: algorithms, analysis, and applications*. Vol. 54. Springer, 2008.
- [12] Sane, Sanjay P., and Michael H. Dickinson. "The control of flight force by a flapping wing: lift and drag production." *Journal of experimental biology* 204, no. 15 (2001): 2607-2626.
- [13] P. Persson, G. Strang, *A Simple Mesh Generator in MATLAB*, *SIAM Review*, Volume 46, Number 2, June 2004, pages 329-345.
- [14] Wood, R. J., S. Avadhanula, R. Sahai, E. Steltz, and R. S. Fearing. "Microrobot design using fiber reinforced composites." *Journal of Mechanical Design* 130 (2008): 052304.
- [15] Xu, Sheng, and Z. Jane Wang. "An immersed interface method for simulating the interaction of a fluid with moving boundaries." *Journal of Computational Physics* 216, no. 2 (2006): 454-493.